Surface orientation and structure of $LaTiO_2N$ nanoparticles

Silviya Ninova,[†,‡] Simone Pokrant,[‡] and Ulrich Aschauer[*,†]

†*Department of Chemistry and Biochemistry, University of Bern, Freiestrasse 3, 3012 Bern, Switzerland*

‡*University Salzburg, Chemistry and Physics of Materials, Jakob-Haringer-Straße 2a, 5020 Salzburg, Austria*

E-mail: ulrich.aschauer@dcb.unibe.ch

Abstract

Perovskite oxynitrides have attracted much attention as visible-light photocatalysts and are primarily used as nanoparticles or in particle-based electrodes for photocatalytic or photoelectrochemical water splitting. The surface termination of these particles will directly impact their catalytic activity and a fundamental understanding of which facets are likely exposed will help in the further optimization of these catalysts. Based on experimental transmission electron microscopy indexing of facets, we calculate, in this work, surface energies of differently reconstructed surfaces and the resulting Wulff shapes using two different approaches. In the first we account for explicit anion order and in the second we treat the anions as fully disordered using the virtual crystal approximation. By comparing experiment and theory, we conclude that a partial anion order is likely to occur at $LaTiO_2N$ surfaces. Moreover our results shows that the anion reordering from *cis* in the bulk to *trans* at the surface as previously suggested for the {001} surface is general, applying also to different surface orientations and re-

constructions. The detailed knowledge of surface structures developed here is a solid foundation on which to computationally explore their relative activity.

Keywords

$LaTiO_2N$, oxynitride, nanoparticle, morphology, surface structure, DFT, TEM

Introduction

Perovskite oxynitrides have attracted significant attention for their promising photocatalytic properties under visible light.[1–3] They maintain a relatively good stability under experimental conditions, similar to their corresponding oxides. At the same time, due to the narrower band gap induced by the less electronegative nitrogen, they absorb a larger portion of the solar spectrum. $LaTiO_2N$ (LTON) is a particularly well-studied oxynitride that is known to successfully split water under visible light, when a sacrificial electron acceptor or a co-catalyst are used to drive the reaction.[4–7] This material has been intensely studied as a photocatalyst in form of nanoparticles[4,5,8] as well as particle-[6,9] and thin-film-based photoanodes.[10,11]

Recent research has established variations in water-splitting performance for different crystal orientations of thin-films photocatalysts.[10] While the surface orientation of thin films can be controlled, i.e via the substrate or the deposition conditions,[10,12] this is not the case when nano-nanoparticle photocatalysts are used. For these photocatalysts, the exposed surfaces are determined either by surface energies or growth velocities of different surface orientations under equilibrium or non-equilibrium conditions respectively. An understanding of the reactivity of a nanoparticle photocatalyst must therefore be based on a knowledge of preferentially occurring facets as well as their relative reactivity. The present work aims to address the first of these requirements by a combination of experiment and theory. While electron microscopy investigations can reliably determine the Miller indices of exposed facets, atomic-scale calculations can provide additional information on the surface structure and

potentially exposed active sites.

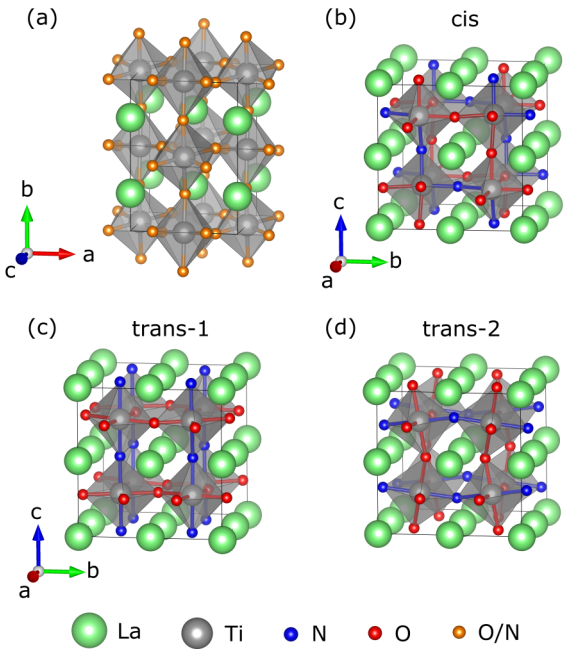

Figure 1: $LaTiO_2N$ in (a) the experimental orthorhombic cell with O/N disorder,[13] and the corresponding pseudo-cubic cell with (b) *cis* as well as (c) and (d) two *trans* anion distributions with different propagation directions of the N-Ti-N chains.

One challenging aspect of oxynitrides such as LTON are different possible arrangements of the oxygen and nitrogen anions in the crystal structure. Previous research has shown that within an octahedral transition metal (TM) unit a *cis* short-range order (Fig. 1b) of the N anions with resulting 90° N-TM-N bonds is favored over a *trans* arrangement (Fig. 1c and d) with 180° N-TM-N bonds. This is rooted in a bonding optimization between the ligands and the TM. The long-range order depends on the arrangement of neighboring octahedral units, where different two-dimensional or three-dimensional arrangements are possible.[14,15] While some oxynitrides order to a certain extent,[15,16] other are inherently disordered.[13] LTON is among the disordered oxyntrides,[13,17] even though some reports suggest the possibility of a partial order.[18,19] We have however recently shown that the anion order at the surface may differ from the one in the bulk, LTON {001} surfaces favoring a 1-2 unit-cell thick *trans* ordered layer due to electrostatic reasons.[20,21]

This (partial) anion disorder, however, renders modeling such materials a challenge, as attaining a sufficiently random distribution, that mimics the lack of long-range order, would require large simulation cell already for the bulk.[22] Calculations of sufficiently thick surface slabs based on these bulk cells would be prohibitively expensive. The most commonly adopted approach to calculate oxynitride bulk[5,17,23–26] and surfaces[20,24,25] consists of constructing and comparing several *cis* or *trans* ordered models that are fully long-range ordered, even if anion vacancies are considered.[27] Cluster expansion[28] with derived special quasi-random (SQS) structures, is one approach to construct structures that are as disordered as possible and which was recently applied to bulk $BaTaO_2N$.[29] An alternative and relatively straightforward approach to treat truly disordered alloys is the virtual crystal approximation (VCA),[30,31] where an appropriately weighted combination (33% N and 67% O character for LTON) of two pseudopotentials is created for the partially occupied site. The VCA was successfully applied to study the dielectric properties of mixed-cation perovskites.[31]

In the present study, we experimentally and theoretically investigate the preferential surface orientations in LTON nanoparticles in thermodynamic equilibrium. Based on the experimental findings, we include less studied oxynitride surface planes with significant surface dipoles that therefore reconstruct. For explicit anion order these dipoles are moreover partially compensated by the anion arrangement in surface layers, while VCA calculations generally yield higher surface energies. We show that neither a fully ordered nor a fully disordered VCA model agrees with experiment and conclude that surfaces are likely to show a partial anion order in experiment.

Methods

DFT calculations

The experimental bulk LTON cell is orthorhombic containing 20-atoms, with a longer b-axis (see Table S1).[13,17] It contains structural distortions, such as the octahedral rotations,[32]

and the anion (dis)order, oxygen and nitrogen forming chemical bonds of different length with titanium. In order to allow for an easier comparison of surface orientations with other perovskite surfaces, we transformed the orthorhombic cell into a pseudo-cubic one, utilizing the transformation matrix

$$\begin{pmatrix} 0.5 & 0 & 0.5 \\ 0 & 1 & 0 \\ -0.5 & 0 & 0.5 \end{pmatrix} \tag{1}$$

which corresponds to a 45°-rotation around the b-axis and a volume doubling, resulting in a 40-atom cell. All surface orientations in this paper use the cubic notation, but we give the conversion between cubic and orthorhombic notation of the considered surface planes in Table S3. Within this cubic unit-cell, we considered both explicit and VCA anion order. For explicit anion order, we considered the models reported in,[20] which differ in *trans* or *cis* nitrogen arrangements and the propagation direction of the Ti-N bonds. We distinguish the *trans*-1 (Figure 1c) and *trans*-2 (Figure 1d) models that differ in geometry (see Table S1) and energy. Since different *cis* models have nearly the same geometries and energies (within 0.1 meV) and also result in surface energies differing at most by 0.05 J/m^2, we consider only a single *cis* model (Figure 1b). For VCA, we occupy all anion sites with 33% N and 67% O, which results in a 0.6% contraction of the lattice compared to experiment (see Table S1).

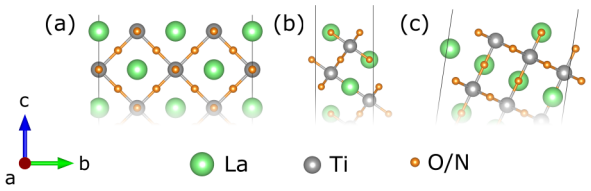

Figure 2: Slab models based on a VCA perovskite structure without octahedral rotations for different pseudo-cubic surface orientations: (a) {011}, (b) {111}, (c) {113}.

Based on these models, we constructed asymmetric surface slabs, with {011}, {111} and {113} surface orientations. The rather low-symmetry bulk crystal structure, in terms of anion order and octahedral rotations, leads to a variety of surface terminations upon cleaving.

This is particularly true for the {111} and {113} surfaces, where it is difficult to clearly define a surface layer. In Figure 2 we, therefore, show the possible terminations for a VCA perovskite structure without octahedral rotations, the actual geometries of all surfaces, including also further reconstructions are presented as insets in the respective figures. We only considered surfaces with low dipoles and no more than half of the metal-anion bonds severed, which avoids high-energy surfaces that would undergo major geometry and/or electronic reconstructions. The relative stability of each surface was evaluated via the surface energy[33]

$$E_{surf} = \frac{2E^{rlx}_{slab} - E^{urlx}_{slab} - E_{bulk}}{2A_{surf}} \tag{2}$$

where E^{rlx}_{slab} and E^{urlx}_{slab} are the total energies of the relaxed and as-cleaved surface, E_{bulk} is the corresponding bulk energy and A_{surf} is the surface area. This definition of E_{surf} allows us to distinguish between the two complementary surface terminations.[20] Due to their different geometry, slabs for different surface orientations differ in the number of atoms. We therefore adjusted the thickness of the slab and the number of unit-cells kept fixed at bulk positions to converge surface energies to within $0.05\,\mathrm{J/m^2}$. Using this approach, the {011} slabs consist of 80 atoms unit cells, where the bottom 20 were kept fixed; the {111} slabs have 30 atoms, where the bottom 10 were kept fixed; and the {113} slabs consist of 60 atoms, where the bottom half were kept fixed. These correspond a slab thickness of $\sim$11 Å, 14 Å and 14 Å, respectively. Reconstructed surfaces were built by moving part of the surface atoms to the bottom surface of the slab at bulk positions.

All bulk and slab geometries were optimized using density functional theory (DFT) with the Quantum ESPRESSO package,[34,35] using the PBE[36] exchange-correlation functional and a Hubbard U correction[37] of 3 eV to the Ti 3d states. Ultra-soft pseudopotentials[38] with La(5s, 5p, 6s, 5d), Ti(3s, 3p, 4s, 3d), O(2s, 2p) and N(2s, 2p) valence states were used for electron-nuclear interactions and wave-functions and the augmented density were expanded in plane waves up to cutoffs of 40 Ry and 320 Ry respectively. The Brillouin zone was sampled using Monkhorst-Pack[39] meshes, adjusted to achieve a precision of 10^{-4} Ry

for the total energy, resulting in 6×4×1 for the {011}, 6×6×1 for the {111} and 6×3×1 for the {113} slabs. The artificial electric field potentially occurring for asymmetric slabs was canceled by a dipole correction[40]. All computational data is available on the NOMAD repository.[41]

Material synthesis and characterization

LTO precursors were prepared by polymerized-complex (PC) synthesis with flux (NaCl/KCl). For the PC synthesis, $Ti\{OCH(CH_3)_2\}_4$ (Sigma-Aldrich, $\geq$ 99.999%), $La(NO_3)_3 \cdot 6\,H_2O$ (Merck, > 99%), $C_6H_8O_7$ (citric acid, Alfa Aesar, $\geq$ 99%), and CH_3OH (methanol, Sigma-Aldrich, puriss) were added to $C_2H_6O_2$ (ethylene glycol, Merck, > 99.5%) with molar ratios of 1/1/6/15/30, respectively. After the complexation under reflux at 80 °C for 4 h, the organic matrix was carbonized at 300 °C. PC-LTO was obtained after calcination at 1000 °C for 6 h. Nitridation reactions of 2 g batches of LTO were performed in an alumina cavity reactor using a NH_3 flow of 200 mL min^{-1} at 950 °C for 16 h in the presence of flux (NaCl/KCl/LTO 0.5/0.5/1 by weight). The PC-LTON-flux samples were quenched to room temperature under an NH_3 atmosphere. The synthesis conditions are the same as reported in Ref.,[7] leading to dense monocrystalline PC-LTON particles with orthorhombic *Imma* structure.[17]

A transmission electron microscope (TEM) with an acceleration voltage of 200 kV (JEOL JEM 2000FS TEM/STEM) was used to assess the morphology and the local crystallinity of the samples in high resolution (HRTEM) mode. Fast Fourier Transforms (FFT) of the HRTEM images were compared to diffraction patterns simulated by the JEMS software.[42] In this way the crystal orientations of the particles were determined based on the orthorhombic crystal structure, including surface orientations of the particles. These orientations were converted to the cubic notation (see SI Section S2) for easy comparison with the theoretically calculated Wulff shapes.

Results

Experimental results

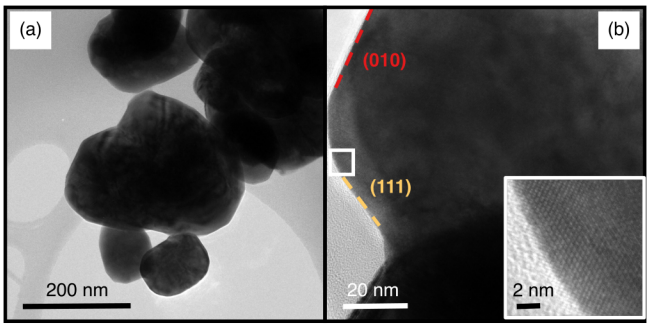

Figure 3: (a) PC-LTON-flux particles; (b) HRTEM image of a particle. The inset corresponds to the magnified image area delimited by the white box demonstrating lattice resolution. Particle facets in cubic notations are marked with red and yellow dashed lines. The FFT pattern is presented in Figure S1.

PC-LTO particles are small (50-300 nm in diameter) and it is therefore reasonable to assume that during ammonolysis, when the atom mobility is enhanced by the addition of flux, largely thermodynamically controlled PC-LTON particle shapes and surfaces are obtained.[7] Overview images of typical agglomerates of PC-LTON-flux particles are presented in Figure 3a) and Figure S1d). The faceted shapes suggest the formation of well-defined surface planes. In total, seven particles were found, where HREM imaging was possible and where the particle orientation was along a main crystallographic axis. Therefore, the results presented here cannot be interpreted in a quantitative manner. However, they give a qualitative indication, which surfaces planes are formed and are therefore thermodynamically stable. Five particles were oriented in the [101] and two in the [111] directions, showing hexagonal diffraction patterns. Correlating the surface plane directions of the particle sides in imaging with the crystallographic directions obtained from the FFT, the surface planes of particles that are vertical to the electron beam direction can be indexed (see Figure S1). We find the following plane families in cubic notation: in [101] direction {011}, {001}, {212}, {111} and $\{\bar{1}3\bar{1}\}$ planes and in [111] direction the {011} plane.

Particle surfaces in viewing direction cannot be indexed with certainty, because TEM does not allow direct conclusions about the thickness of the particles. However, all particles studied by HRTEM exhibit constant contrast over the entire particle area indicating a constant thickness. Therefore, it is safe to assume, that the upper and lower surfaces of the particles deposited on the TEM grid are composed of planes perpendicular to the viewing directions. Based on this assumption these surfaces can be indexed as well. Following this methodology, the particles' top and bottom facets consist of {011} or {111} planes. To summarize: we have observed {011}, {011}, {111}, {113} and to a smaller extent {212} planes.

Explicit-order surfaces

The anion order in oxynitrides can have a significant impact on their surface stability. We have previously shown that LTON-{001} slabs have a *trans* surface anion distribution that differs from the *cis*-ordered bulk.[20] This was governed by the formation of polar-compensated (LaN and TiO_2) atomic layers for the *trans*-order. In the following, we investigate how the anion order affects the stability of other experimentally frequently observed surface orientations of LTON nanoparticles, namely the {011}, {111}, and {113} surface orientations.

{011} surfaces

An as-cleaved {011} LTON surface can yield two terminations - LaTiX and XX, where X corresponds to either O or N (see Figure 2a) and insets in Figure 4). For explicit anion occupations, the following terminations are possible, where we group complementary terminations separated by slashes: LaTiN/OO, LaTiO/ON and $LaTi(O_{0.5}N_{0.5})/O_{1.5}N_{0.5}$. The least charged layers occur, when all N atoms are in the LaTi-plane (LaTiN/OO), resulting in nominal layer charges (in e/unit cell) of +4/-4, the other possibilities resulting in even higher layer charges (+5/-5 for LaTiO/ON and +4.5/-4.5 for $LaTi(O_{0.5}N_{0.5})/O_{1.5}N_{0.5}$). Consequently we expect high surface dipoles and hence high surface energies for all as-cleaved

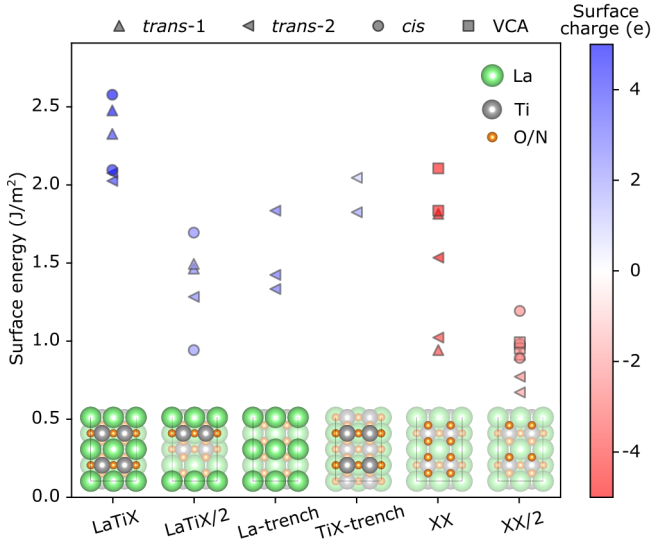

Figure 4: Computed LTON {011} surface energies for different surface reconstructions and anion orders. Some reconstructions have more than one point per model, which reflects the different symmetrically inequivalent surface planes. The coloring of the data points reflects their nominal surface charge according to the color bar on the right. Numerical values for surface energies and nominal charges can be found in Table S4.

surfaces and - guided by similar studies for perovskite oxides[33,43,44] - introduce surface reconstructions to lower the dipoles and surface energies (see insets in Figure 4). From the as-cleaved LaTiX, we can obtain surfaces with half-layers (LaTiX/2) or La/TiX-trenches, while the XX termination can only be stabilized half-layers (XX/2). The resulting surface energies for all considered terminations and anion orders are summarized in Figure 4, where we also indicate the nominal charge of the surface layer.

We observe that the surface energy strongly depends on the termination. The general trend is to have higher surface energies for cation-containing surfaces, as compared to the anion-terminated ones. The surface energy for the (LaTiN) trans-2 model is 2.02 J/m^2 as opposed to 1.02 J/m^2 for the complementary (OO) termination. This result is, however, not surprising, since this particular termination has a high surface dipole and the cations are likely to shift from their bulk position to partly compensate the dipole. On the contrary, oxygen and nitrogen can easily move within the perovskite structure of the topmost atomic layers, for instance via deviations in the octahedral rotation angles, which reduces the surface

dipole and stabilizes the surface termination.

The La- and TiX-trench reconstructions stabilize the *trans*-2 LaTiX slab by 0.74 J/m^2 and 0.25 J/m^2, respectively. The LaTiX/2 reconstruction on the other hand leads to low surface energies for the *cis* ordered slab. The surfaces with the lowest energy are however the anion-terminated surfaces, the one with a half-atomic layer reconstruction (trans-2 OO/2) being most stable at 0.67 J/m^2. Such a reconstruction was also reported most stable for perovskite oxides that prefer the anion termination over the metal-containing plane.[43,45,46]

We want to note that the XX termination can, in particular for high N concentrations at the surface, lead to formation of N_2 dimers that either remain bound to Ti or desorb. These findings are in agreement with experimentally observed nitrogen depletion.[4,19] As dimer formation invalidates our formulation of the surface energy, such cases were excluded from the reported results. Dimer formation was not observed for XX/2, likely due to the larger separation between the surface anions.

Overall, we can see that reconstructions significantly affect the surface energy, the half-layer anion reconstruction (XX/2) occurring with the highest probability. The effect of the anion-order is less pronounced, even though in most cases the *trans*-2 order is among the lowest-energy slabs but other anion orders result in very similar surface energies.

{111} surfaces

As-cleaved {111} perovskite surfaces are strongly polar and expected to reconstruct. For perovskite oxides, the {111} surface structure was shown to strongly depend on the experimental conditions[47–49] and it was even possible to suppress severe reconstructions.[50] For $SrTiO_3$ two distinct termination of micrometer scale with different polarity were observed at high temperatures.[51] From theory as-cleaved[52–54] as well as reconstructed {111} perovskite oxide surfaces were studied[46,48,55,56] and it was established that as-cleaved surfaces are less stable.[46,56] For LTON the stacking sequence along the [111] direction is LaX_3/Ti and we consider reconstructions in the LaX_3 layer that differ in La and/or X content of the topmost

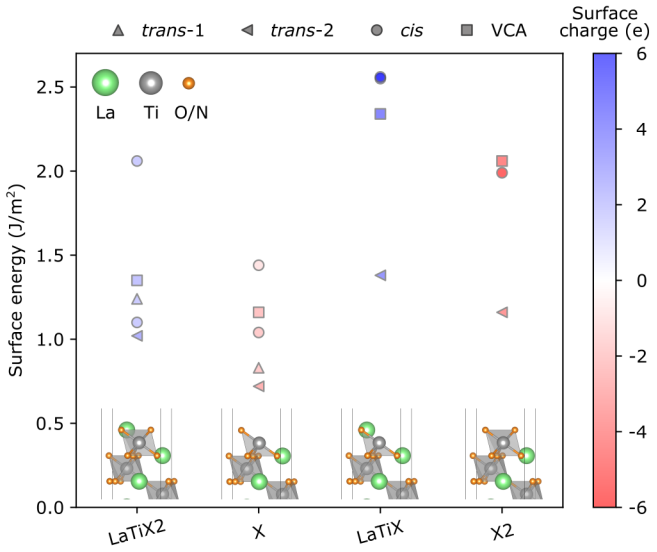

Figure 5: Computed LTON {111} surface energies for different surface reconstructions and anion orders. Some reconstructions have more than one point per model, which reflects the different symmetrically inequivalent surface planes. The coloring of the data points reflects their nominal surface charge according to the color bar on the right, where the surface comprises all atoms above the topmost two La/Ti atoms. Numerical values for surface energies and nominal charges can be found in Table S5.

layer (see insets in Figure 5). We do not consider the as-cleaved (LaTiX3) surfaces, since based on the above discussion, we expect them to be less stable.

Among the investigated surface slabs (see Figure 5), we find a good correlation of the surface charge and hence the surface dipole with the surface energy, the less charged X and LaTiX2 reconstructions being more stable than the more polar LaTiX and X2 reconstructions. Similarly to the {011} slabs, the purely anion-terminated surface (X) has a lower surface energy compared to the one also containing La. In addition to its high energy we note that the X2 reconstruction with two N-atoms promotes N_2 formation (see Table S5), which is the case for the *cis* model, analogously to the {011}-slabs. The *trans*-2 anion order seems to be favored for this surface as the lowest surface energy for all reconstructions is obtained with that anion order, other orders being at least 0.08 J/m^2 higher in energy (see Table S5). The overall most preferential termination is the *trans*-2 X at 0.72 J/m^2, where the titanium is coordinated by two N and two O atoms.

{113} surfaces

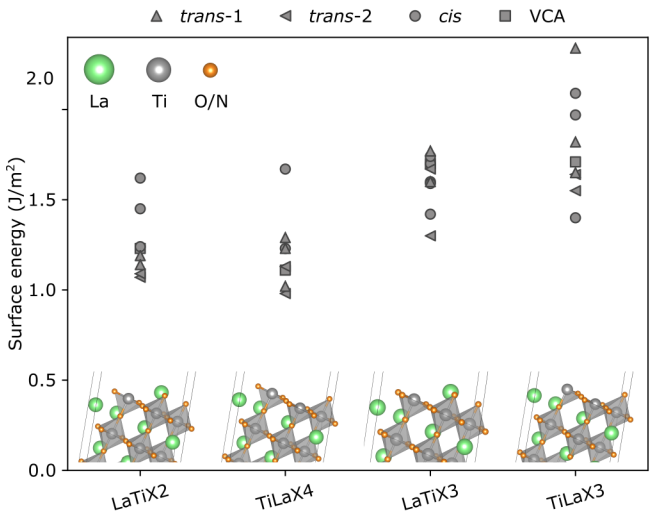

Figure 6: Computed LTON {113} surface energies for different surface reconstructions and anion orders. Some reconstructions have more than one point per model, which reflects the different symmetrically inequivalent surface planes. Numerical values for surface energies and nominal charges can be found in Table S6.

The {113} orientation appears as a vicinal surface, when transitioning from {001} to {111} surface. The octahedral rotations do not allow for a clear separation into layers compared to other LTON surface orientations in this study and also compared to less distorted pure oxides.[57] We thus consider several possible chemical terminations, which comprise the formation of 3-, 4- and 5-coordinated Ti-atoms at the surface layer (see insets in Figure 6) but are not able to characterize the nominal charge in the surface layer. Similarly to the other two investigated surfaces, the *trans* anion order again yields the lowest-energy slabs for all but the LaTiX3 reconstruction (see Figure 6). The *trans*-2 TiLaX4 has a surface energy of 0.98 J/m^2, which is higher than for the other surface orientations.

VCA surfaces

Above we have established surface energies with explicit anion order, implying perfect long-range order of the anions. Here we will investigate the other extreme of a full anion disorder

via the VCA with 33% N and 67% O on all anion sites. Compared to the above explicit anion order calculations, we expect to miss the polarity compensation due to preferential anion orders as well as geometry differences resulting from different Ti-O and Ti-N bond lengths.

The computed surface energies are reported in Table S7 and are shown as square symbols in Figures 4, 5 and 6. We observe that for all surface orientation the VCA and the explicit anion order yield the same lowest energy reconstruction. This implies that the reconstruction plays a more important role than the anion order. The VCA surface energies are always higher than the ones with explicit anion order, implying that the explicit order allows to reduce small dipoles remaining after reconstructing. We note that when an explicit anion order would allow for an ideal polarity compensation, such as for {001} surfaces,[20] then the VCA-imposed charging of layers leads to the largest increase in surface energy. This results, at the VCA level, in a higher energy of the {001} surface than a suitably reconstructed {011} surface, which contradicts the trend of low {001} surface energies for perovskite oxides compared to more polar surface orientations.[43,44]

Particle shape

The surface energies of the different possible surface planes determine the particle shape in thermodynamic equilibrium according to the Wulff construction.[58] In this section we will use the surface energies computed here with explicit anion order and the VCA as well as our previously computed {001} surface energies with explicit anion order[20] to predict equilibrium particle shapes with and without long-range anion order. These particle shapes consider only 0K DFT surface energies, without accounting for chemical potential or temperature effects.

From the data summarized in Figure 7 we can see that for explicit anion order {001} is the lowest energy surface, followed by {011}, {111} and {113} all with a *trans*-2 anion order. A similar trend has been established for other perovskite oxides.[53] The VCA on the other hand favors, as discussed above, a suitably reconstructed {011} surface over the {001} surface,

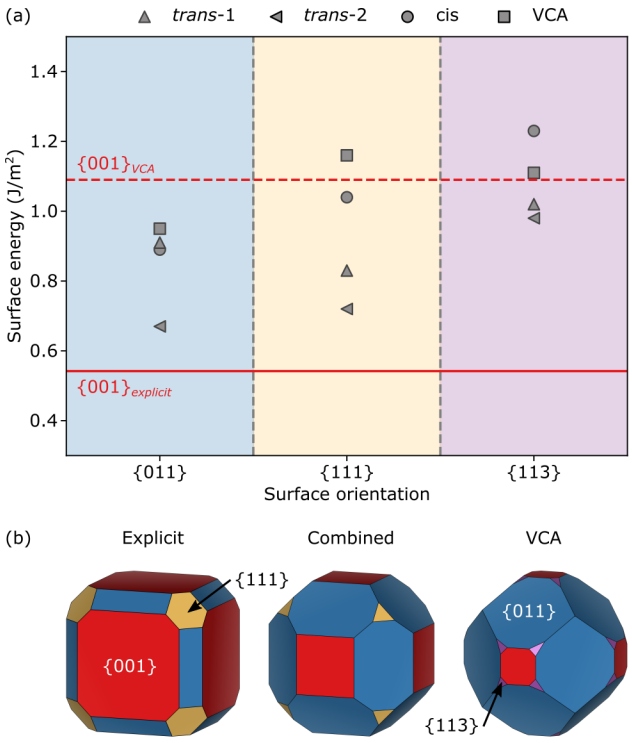

Figure 7: (a) Surface energies for the lowest energy reconstruction of each explicit and VCA anion order and for the different surface orientations. Numerical values can be found in Tables S4, S5, S6 and S7 as well as in Ref.[20] (b) Resulting Wulff shapes for the lowest-energy explicit anion order and the VCA as well as one combining explicit and VCA surface energies at equal ratios. The color of facets corresponds to the background shading in panel (a).

followed by the {113} and the {111} surface. This already implies that the particle shapes will look fairly different as shown in Figure 7(b). Comparing with experiment (see Figure 3), only the Wulff shape with explicit anion order displays particles with {001} and {111} facets that were experimentally indexed (see Figure 3). On the other hand, the fact {011} and {113} facets were indexed as well would be in better agreement with the VCA results. This reasoning would imply that experimentally neither the full long-range anion order of the explicit model not the full disorder of the VCA model occurs but an intermediate situation with partial anion order (depicted as the center model in Figure 7(b) assuming a combination of surfaces energies at equal ratios), that allows for the simultaneous appearance of all four facets. Besides a partial anion order, also the high synthesis temperature could lead to the appearance of additional facets in the equilibrium morphology, since finite temperature is generally expected to lead to less faceted morphologies.

Conclusions

We have investigated the exposed surface facets of equilibrium-shaped $LaTiO_2N$ nanoparticles experimentally and theoretically. Experiment found primarily {001}, {011}, {111} and {113} surfaces that were subsequently computed using density functional theory (DFT). We considered both an explicit anion order that may reduce the surface energy by partially compensating polarity and the virtual crystal approximation (VCA) that treats a full anion disorder. We find that all surfaces but the {001} reconstruct to reduce the surface dipole, the explicit anion order resulting in a further lowering of the surface energy. Disordered VCA structures are always higher in energy and stabilize the {011} over the {001} surface. By comparing the experimental particle shape with the computed Wulff shape, we conclude that experimental particles are likely to display partial anion order at the surface such that the {111} facet can appear while also allowing for {011} and {113} facets in the morphology. Since the *trans* anion order generally results in lower surface energies than the *cis* anion

order, we conclude that the previously proposed anion reordering at $LaTiO_2N$ surfaces also applies to other surface orientations as well as reconstructed surfaces. The knowledge gained here for likely atomic-scale surface structures forms a foundation on which to explore their relative photocatalytic activity.

Acknowledgement

This research was funded by the SNF Professorship Grant PP00P2_157615. Calculations were performed on UBELIX (http://www.id.unibe.ch/hpc), the HPC cluster at the University of Bern.

Supporting Information Available

Additional bulk geometry information, crystallographic conversion table, FFT patterns and numerical values for surface energies.

References

(1) Takata, T.; Pan, C.; Domen, K. Recent progress in oxynitride photocatalysts for visible-light-driven water splitting. *Sci. Technol. Adv. Mater* **2015**, *16*, 033506.

(2) Ahmed, M.; Xinxin, G. A review of metal oxynitrides for photocatalysis. *Inorg. Chem. Front.* **2016**, *3*, 578–590.

(3) Pokrant, S.; Maegli, A. E.; Chiarello, G. L.; Weidenkaff, A. Perovskite-related oxynitrides in photocatalysis. *CHIMIA* **2013**, *67*, 162–167.

(4) Kasahara, A.; Nukumizu, K.; Hitoki, G.; Takata, T.; Kondo, J. N.; Hara, M.; Kobayashi, H.; Domen, K. Photoreactions on $LaTiO_2N$ under visible light irradiation. *J. Phys. Chem. A* **2002**, *106*, 6750–6753.

(5) Kasahara, A.; Nukumizu, K.; Takata, T.; Kondo, J. N.; Hara, M.; Kobayashi, H.; Domen, K. $LaTiO_2N$ as a visible-light ($\leq$600 nm)-driven photocatalyst (2). *J. Phys. Chem. B* **2003**, *107*, 791–797.

(6) Leroy, C. M.; Maegli, A. E.; Sivula, K.; Hisatomi, T.; Xanthopoulos, N.; Otal, E. H.; Yoon, S.; Weidenkaff, A.; Sanjines, R.; Grätzel, M. $LaTiO_2N/In_2O_3$ photoanodes with improved performance for solar water splitting. *ChemComm* **2012**, *48*, 820–822.

(7) Maegli, A. E.; Pokrant, S.; Hisatomi, T.; Trottmann, M.; Domen, K.; Weidenkaff, A. Enhancement of photocatalytic water oxidation by the morphological control of $LaTiO_2N$ and cobalt oxide catalysts. *J. Phys. Chem. C* **2014**, *118*, 16344–16351.

(8) Rugen, E. E.; Koczkur, K. M.; Skrabalak, S. E. Facile synthesis of porous LaTiO and $LaTiO_2N$ microspheres. *Dalton Trans.* **2017**, *46*, 10727–10733.

(9) Landsmann, S.; Maegli, A. E.; Trottmann, M.; Battaglia, C.; Weidenkaff, A.; Pokrant, S. Design guidelines for high-performance particle-based photoanodes for water splitting: Lanthanum titanium oxynitride as a model. *ChemSusChem* **2015**, *8*, 3451–3458.

(10) Pichler, M.; Si, W.; Haydous, F.; Téllez, H.; Druce, J.; Fabbri, E.; Kazzi, M. E.; Döbeli, M.; Ninova, S.; Aschauer, U.; Wokaun, A.; Pergolesi, D.; Lippert, T. $LaTiO_xN_y$ thin film model systems for photocatalytic water splitting: Physicochemical evolution of the solidliquid interface and the role of the crystallographic orientation. *Adv. Funct. Mater.* **2017**, *27*, 1605690.

(11) Haydous, F.; Döbeli, M.; Si, W.; Waag, F.; Li, F.; Pomjakushina, E.; Wokaun, A.; Gökce, B.; Pergolesi, D.; Lippert, T. Oxynitride thin films versus particle-based photoanodes: A comparative study for photoelectrochemical solar water splitting. *ACS Appl. Energy Mater.* **2019**, *2*, 754–763.

(12) Paven-Thivet, C. L.; Gendre, L. L.; Castrec, J. L.; Cheviré, F.; Tessier, F.; Pinel, J. Oxynitride perovskite $LaTiO_xN_y$ thin films deposited by reactive sputtering. *Prog. Solid State Chem.* **2007**, *35*, 299 – 308.

(13) Clarke, S. J.; Guinot, B. P.; Michie, C. W.; Calmont, M. J. C.; Rosseinsky, M. J. Oxynitride perovskites: Synthesis and structures of $LaZrO_2N$, $NdTiO_2N$, and $LaTiO_2N$ and comparison with oxide perovskites. *Chem. Mater.* **2002**, *14*, 288–294.

(14) Fuertes, A. Prediction of anion distributions using Pauling's second rule. *Inorg. Chem.* **2006**, *45*, 9640–9642.

(15) Yang, M.; Oró-Solé, J.; Rodgers, J. A.; Jorge, A. B.; Fuertes, A.; Attfield, J. P. Anion order in perovskite oxynitrides. *Nat. Chem.* **2011**, *3*, 47.

(16) Page, K.; Stoltzfus, M. W.; Kim, Y.-I.; Proffen, T.; Woodward, P. M.; Cheetham, A. K.; Seshadri, R. Local atomic ordering in $BaTaO_2N$ studied by neutron pair distribution function analysis and density functional theory. *Chem. Mater.* **2007**, *19*, 4037–4042.

(17) Yashima, M.; Saito, M.; Nakano, H.; Takata, T.; Ogisu, K.; Domen, K. *Imma* perovskite-type oxynitride $LaTiO_2N$: structure and electron density. *ChemComm* **2010**, *46*, 4704–4706.

(18) Logvinovich, D.; Bocher, L.; Sheptyakov, D.; Figi, R.; Ebbinghaus, S. G.; Aguiar, R.; Aguirre, M. H.; Reller, A.; Weidenkaff, A. Microstructure, surface composition and chemical stability of partly ordered $LaTiO_2N$. *Solid State Sci.* **2009**, *11*, 1513 – 1519.

(19) Chen, D.; Habu, D.; Masubuchi, Y.; Torii, S.; Kamiyama, T.; Kikkawa, S. Partial nitrogen loss in $SrTaO_2N$ and $LaTiO_2N$ oxynitride perovskites. *Solid State Sci.* **2016**, *54*, 2 – 6.

(20) Ninova, S.; Aschauer, U. Surface structure and anion order of the oxynitride $LaTiO_2N$. *J. Mat. Chem. A* **2017**, *5*, 11040–11046.

(21) Ninova, S.; Aschauer, U. Anion-order driven polar interfaces at $LaTiO_2N$ surfaces. *J. Mat. Chem. A* **2019**, *7*, 2129–2134.

(22) Fang, C.; de Wijs, G.; Orhan, E.; de With, G.; de Groot, R.; Hintzen, H.; Marchand, R. Local structure and electronic properties of $BaTaO_2N$ with perovskite-type structure. *J. Phys. Chem. Solids* **2003**, *64*, 281 – 286.

(23) Ziani, A.; Le Paven, C.; Le Gendre, L.; Marlec, F.; Benzerga, R.; Tessier, F.; Cheviré, F.; Hedhili, M. N.; Garcia-Esparza, A. T.; Melissen, S.; Sautet, P.; Le Bahers, T.; Takanabe, K. Photophysical properties of $SrTaO_2N$ thin films and influence of anion ordering: A joint theoretical and experimental investigation. *Chem. Mater.* **2017**, *29*, 3989–3998.

(24) Kubo, A.; Giorgi, G.; Yamashita, K. Anion ordering in $CaTaO_2N$: Structural impact on the photocatalytic activity. Insights from first-principles. *Chem. Mater.* **2017**, *29*, 539–545.

(25) Ouhbi, H.; Aschauer, U. Water oxidation chemistry of oxynitrides and oxides: Comparing $NaTaO_3$ and $SrTaO_2N$. *Surf. Sci.* **2018**, *677*, 258 – 263.

(26) Garcia-Esparza, A. T.; Tymińska, N.; Al Orabi, R. A. R.; Le Bahers, T. Full in silico DFT characterization of lanthanum and yttrium based oxynitride semiconductors for solar fuels. *J. Mat. Chem. C* **2019**, *7*, 1612–1621.

(27) Wang, X.; Li, Z.; Zou, Z. A hybrid density functional theory study of the anion distribution and applied electronic properties of the $LaTiO_2N$ semiconductor photocatalyst. *PCCP* **2015**, *17*, 19631–19636.

(28) Sanchez, J.; Ducastelle, F.; Gratias, D. Generalized cluster description of multicomponent systems. *Physica A* **1984**, *128*, 334 – 350.

(29) Xu, X.; Jiang, H. First-principles investigation on anion order, electronic structure and dielectric properties of $BaTaO_2N$. *J. Mat. Chem. A* **2019**, *7*, 14583–14591.

(30) Nordheim, L. Zur Elektronentheorie der Metalle. I. *Ann. Phys.* **1931**, *401*, 607–640.

(31) Bellaiche, L.; Vanderbilt, D. Virtual crystal approximation revisited: Application to dielectric and piezoelectric properties of perovskites. *Phys. Rev. B* **2000**, *61*, 7877–7882.

(32) Attfield, J. P. Principles and applications of anion order in solid oxynitrides. *Cryst. Growth Des.* **2013**, *13*, 4623–4629.

(33) Eglitis, R. I.; Vanderbilt, D. Ab initio calculations of $BaTiO_3$ and $PbTiO_3$ (001) and (011) surface structures. *Phys. Rev. B* **2007**, *76*, 155439.

(34) Giannozzi, P.; Baroni, S.; Bonini, N.; Calandra, M.; Car, R.; Cavazzoni, C.; Ceresoli, D.; Chiarotti, G. L.; Cococcioni, M.; Dabo, I.; Dal Corso, A.; de Gironcoli, S.; Fabris, S.; Fratesi, G.; Gebauer, R.; Gerstmann, U.; Gougoussis, C.; Kokalj, A.; Lazzeri, M.; Martin-Samos, L.; Marzari, N.; Mauri, F.; Mazzarello, R.; Paolini, S.; Pasquarello, A.; Paulatto, L.; Sbraccia, C.; Scandolo, S.; Sclauzero, G.; Seitsonen, A. P.; Smogunov, A.; Umari, P.; Wentzcovitch, R. M. QUANTUM ESPRESSO: a modular and open-source software project for quantum simulations of materials. *J. Phys. Condens. Matter* **2009**, *21*, 395502.

(35) Giannozzi, P.; Andreussi, O.; Brumme, T.; Bunau, O.; Nardelli, M. B.; Calandra, M.; Car, R.; Cavazzoni, C.; Ceresoli, D.; Cococcioni, M.; Colonna, N.; Carnimeo, I.; Corso, A. D.; de Gironcoli, S.; Delugas, P.; Jr, R. A. D.; Ferretti, A.; Floris, A.; Fratesi, G.; Fugallo, G.; Gebauer, R.; Gerstmann, U.; Giustino, F.; Gorni, T.; Jia, J.; Kawamura, M.; Ko, H.-Y.; Kokalj, A.; Kkbenli, E.; Lazzeri, M.; Marsili, M.; Marzari, N.; Mauri, F.; Nguyen, N. L.; Nguyen, H.-V.; de-la Roza, A. O.; Paulatto, L.; Ponc, S.; Rocca, D.; Sabatini, R.; Santra, B.; Schlipf, M.; Seitsonen, A. P.; Smogunov, A.; Timrov, I.; Thonhauser, T.; Umari, P.; Vast, N.; Wu, X.; Baroni, S. Ad-

vanced capabilities for materials modelling with QUANTUM ESPRESSO. *J. Phys. Condens. Matter* **2017**, *29*, 465901.

(36) Perdew, J. P.; Burke, K.; Ernzerhof, M. Generalized gradient approximation made simple. *Phys. Rev. Lett.* **1996**, *77*, 3865–3868.

(37) Anisimov, V. I.; Zaanen, J.; Andersen, O. K. Band theory and Mott insulators: Hubbard U instead of Stoner I. *Phys. Rev. B* **1991**, *44*, 943–954.

(38) Vanderbilt, D. Soft self-consistent pseudopotentials in a generalized eigenvalue formalism. *Phys. Rev. B* **1990**, *41*, 7892–7895.

(39) Monkhorst, H. J.; Pack, J. D. Special points for Brillouin-zone integrations. *Phys. Rev. B* **1976**, *13*, 5188–5192.

(40) Bengtsson, L. Dipole correction for surface supercell calculations. *Phys. Rev. B* **1999**, *59*, 12301–12304.

(41) Ninova, S.; Aschauer, U. $LaTiO_2N$ nanoparticle surfaces. 2020; Data available on the NOMAD repository, `https://dx.doi.org/10.17172/NOMAD/2020.05.14-1`.

(42) Stadelmann, P. JEMS Software. `http://www.jems-saas.ch/`, Accessed: 01-08-2019.

(43) Heifets, E.; Ho, J.; Merinov, B. Density functional simulation of the $BaZrO_3$ (011) surface structure. *Phys. Rev. B* **2007**, *75*, 155431.

(44) Eglitis, R. I.; Vanderbilt, D. Ab initio calculations of the atomic and electronic structure of $CaTiO_3$ (001) and (011) surfaces. *Phys. Rev. B* **2008**, *78*, 155420.

(45) Eglitis, R. I.; Rohlfing, M. First-principles calculations of the atomic and electronic structure of $SrZrO_3$ and $PbZrO_3$ (001) and (011) surfaces. *J. Phys. Condens. Matter* **2010**, *22*, 415901.

(46) Wang, Y.; Cheng, J.; Behtash, M.; Tang, W.; Luo, J.; Yang, K. First-principles studies of polar perovskite $KTaO_3$ surfaces: structural reconstruction, charge compensation, and stability diagram. *PCCP* **2018**, *20*, 18515–18527.

(47) Chiaramonti, A. N.; Lanier, C. H.; Marks, L. D.; Stair, P. C. Time, temperature, and oxygen partial pressure-dependent surface reconstructions on $SrTiO_3$(111): A systematic study of oxygen-rich conditions. *Surf. Sci.* **2008**, *602*, 3018 – 3025.

(48) Marks, L. D.; Chiaramonti, A. N.; Tran, F.; Blaha, P. The small unit cell reconstructions of $SrTiO_3$(111). *Surf. Sci.* **2009**, *603*, 2179 – 2187.

(49) Feng, J.; Zhu, X.; Guo, J. Reconstructions on $SrTiO_3$(111) surface tuned by Ti/Sr deposition. *Surf. Sci.* **2013**, *614*, 38 – 45.

(50) Blok, J. L.; Wan, X.; Koster, G.; Blank, D. H. A.; Rijnders, G. Epitaxial oxide growth on polar (111) surfaces. *Appl. Phys. Lett.* **2011**, *99*, 151917.

(51) Zhu, Y.; Salvador, P. A.; Rohrer, G. S. Controlling the relative areas of photocathodic and photoanodic terraces on the $SrTiO_3$(111) surface. *Chem. Mater.* **2016**, *28*, 5155–5162.

(52) Pojani, A.; Finocchi, F.; Noguera, C. A theoretical study of the unreconstructed polar (111) face of $SrTiO_3$. *Appl. Surf. Sci.* **1999**, *142*, 177 – 181.

(53) Eglitis, R. I. Comparative first-principles calculations of $SrTiO_3$, $BaTiO_3$, $PbTiO_3$ and $CaTiO_3$ (001), (011) and (111) surfaces. *Ferroelectrics* **2015**, *483*, 53–67.

(54) Eglitis, R. I. Ab initio hybrid DFT calculations of $BaTiO_3$, $PbTiO_3$, $SrZrO_3$ and $PbZrO_3$ (111) surfaces. *Appl. Surf. Sci.* **2015**, *358*, 556 – 562.

(55) Pojani, A.; Finocchi, F.; Noguera, C. Polarity on the $SrTiO_3$ (111) and (110) surfaces. *Surf. Sci.* **1999**, *442*, 179 – 198.

(56) Liu, W.; Wang, C.; Cui, J.; Man, Z.-Y. Ab initio calculations of the $CaTiO_3$ (111) polar surfaces. *Solid State Commun.* **2009**, *149*, 1871 – 1876.

(57) Ouhbi, H.; Aschauer, U. Water oxidation catalysis on reconstructed $NaTaO_3$ (001) surfaces. *J. Mat. Chem. A* **2019**, *7*, 16770–16776.

(58) Wulff, G. Zur Frage der Geschwindigkeit des Wachsthums und der Auflösung der Krystallflächen. *Z. Kristallogr. Cryst. Mater.* **1901**, *34*, 449–530.

Graphical TOC Entry